Deep learning-driven analysis for cellular structure characteristics of spherical premixed hydrogen-air flames

Gengxin Zhang [a], Hongming Xu [a,*], Dawei Wu [a], Junfeng Yang [b], Mohamed E. Morsy [b], Mehdi Jangi [a], Roger Cracknell [c], Wookyung Kim [d]

[a] Department of Mechanical Engineering, School of Engineering, University of Birmingham, Edgbaston, Birmingham, B15 2TT, UK
[b] School of Mechanical Engineering, University of Leeds, Leeds, LS2 9JT, UK
[c] Shell Global Solutions UK, Shell Centre, London, SE1 7NA, UK
[d] Department of Mechanical Systems Engineering, Hiroshima University, 1-4-1 Kagamiyama, Higashi-Hiroshima, Hiroshima, 739-8527, Japan

ABSTRACT

The extraction of cellular structure feature on the spherical premixed flame surface faces accuracy challenges. The Schlieren technique was employed to obtain the hydrogen-air premixed spherical flames images in a constant volume vessel at room temperature and atmospheric pressure under an equivalent ratio of 0.8 in this work. A bio-inspired Cellpose 2.0, driven by deep learning, is innovatively introduced to train the cell segmentation model in the combustion field. After labeling and training cells of different shapes and sizes, an efficient and accurate model suitable for cell feature extraction was finally obtained to identify and quantify various cells characteristics, such as number, size, and distribution. Results show that the average precision (AP) during the model online pre-training process reaches 0.625. Meanwhile, the critical flame radius of transition acceleration obtained is 36 mm and the crack length tends to grow linearly after the flame radius exceeds this critical point. Additionally, the average cell area gradually converges to a stable value after the flame radius exceeds the uniform cellularity critical radius. The cell segmentation model obtained in this work can be further used to train different spherical flames under various conditions, helping to develop hydrogen combustion and explosion modelling.

1. Introduction

In the context of carbon neutrality, the zero-carbon fuel hydrogen plays an important role in the decarbonisation of combustion [1,2]. The propagation of premixed hydrogen-air flames in combustion chambers could be influenced by the intrinsic instability, leading to combustion oscillations, flame acceleration, and even explosions [3]. The intrinsic instability within premixed flames originates from combustion dynamics, including the competition between the diffusion of mass and heat (thermal-diffusion instability), the differences between the burnt and unburnt gases (hydrodynamic instability), and the body force exerted by the density gradients of the premixed flames (buoyancy instability) [4]. However, stable flame propagation can often ensure the safe combustion and utilization of hydrogen energy [5]. Therefore, researchers have begun to focus on the impact of instability on the propagation of premixed flames.

At present, researchers have conducted studies on spherical premixed combustion flames for various traditional fuels, bio-substitute fuels, low-carbon and zero-carbon fuels, and multi-component mixed gases [6–9]. An interesting cellularization phenomenon accompanies with the flame propagation, transitioning from laminar to self-accelerating, self-similar, and eventually to self-turbulent [10,11]. The cellularization of a flame refers to the process where a flame transitions from a laminar state to a surface with irregular cellular structures. These structures become noticeable upon reaching a certain critical size, known as the critical radius. Typically, three onsets of cellular instability are clearly distinguished by Zhao et al., including the crack initiation, transition acceleration and uniform cellularity [12,13]. Moreover, the critical Peclet number is the critical hydrodynamic length scale, i.e. critical flame radius, normalized by the flame length scale, i.e. flame thickness, which measures the intensity of hydrodynamic instability [14]. Additionally, there are other parameters that can be used to characterize the intrinsic instability in premixed flames, such as thermal expansion ratio, Lewis number, stretch rate, Karlovitz number,

Markstein length and number, etc. [7] Accurate determination of these parameters is crucial for understanding and predicting flame propagation behavior. Kim et al. have extensively studied cell instability in expanding spherical flames of hydrogen-air, methane-air, and propane-air mixtures. They established the critical values of flame radius and Peclet numbers, showing that these critical values increase with fuel concentration but decrease with initial pressure [15]. Subsequently, they studied flame self-acceleration and self-similarity, providing insights into the flame fractal features and their behaviors in accidental explosions [16,17]. Xie et al. developed empirical formulas for critical Peclet and Karlovitz numbers, greatly enhancing understanding of flame behavior under different conditions [18]. Zhao et al. systematically analyzed the accelerative propagation of laminar and turbulent premixed hydrogen-air flames inside a chamber. They discovered that the laminar flame propagation process is divided into three phases: quasi-steady, transitional acceleration, and saturated acceleration, with the acceleration almost remaining constant during the saturated acceleration phase. Turbulent flame propagation, on the other hand, follows a continuous acceleration law and is easily influenced by the intensity of turbulence [19]. As mentioned above, few researchers have quantitatively focused on the cellular structure of the spherical flame surface, which is closely related to the flame propagation speed. Therefore, quantitatively obtaining the cellular structure characteristics of spherical premixed hydrogen-air flames is crucial for the development of predictive models for hydrogen combustion. The extraction of cell structure features is inseparable from image processing technology. Currently, some quantitative analyses using image processing mainly focus on the definition and calculation of the flame equivalent radius. Han et al. compared four typical calculation methods and their adaptability for radius measurement. The results showed that more accurate flame radius calculation methods have a positive effect on eliminating errors in laminar burning velocity and Markstein length [20]. In addition to the above-mentioned methods of flame radius fitting, researchers often use equal area (pixels) to define the equivalent flame radius [21]. Zhang et al. investigated the effects of the hydrogen fractions and equivalence ratios on the local radius and pulsation radius of the flame front, and the perturbations at different flame positions were quantitatively analyzed [22]. The wavelet transform was further utilized to decompose disturbances with different scales in the flame front. For a quantitative analysis of the flame's geometric structure, parameters such as the maximum and minimum rates of fluctuation radius growth, the growth rate of the fluctuation range, and the energy of the decomposition components were defined. The findings revealed that disturbances of various scales are significantly amplified as the flame develops [23]. Additionally, some studies also used image processing technology to directly obtain the cell size of two-dimensional shadow images quantitatively. Kim et al. used image processing to quantitatively characterize the cells size distributed on part of the flame images, finding that the cell size generated by hydrodynamic instability is larger than that generated by diffusion thermal instability [15]. Wu et al. studied the cellularization process of methanol-hydrogen flames to understand the transition from laminar to turbulent flames. In their work, the two-dimensional (2D) average cell area was defined using image processing technology as an indicator to assess flame instability, which decreased slightly after fully cellularization [24]. Similarly, Li et al. also treated the flame as two-dimensional and quantitatively obtained the number of cells on the flame surface, the area of each cell, and the average cell area using image processing technology to characterize the instability of the flame [25]. In order to obtain more accurate quantitative information about the cellular structure on the surface of spherical flames, the Future Engines and Fuels Lab at the University of Birmingham was the first institute to propose a more refined and digitalized concept of image processing, addressing the issue of 2D projected cell areas being smaller than actual values with the three-dimensional (3D) reconstruction of cell areas [26]. Later on, Xu et al. implemented this 3D reconstruction concept and conducted some work on different

components of substitute fuels and continuously improved image processing techniques in this process [27–29]. The watershed algorithm was their main image segmentation technique, achieving relatively good cell segmentation results [30,31]. Indeed, traditional segmentation methods are largely based on pixel intensity and spatial relationships, with a strong subjective component to code adaptation, and their development has reached a bottleneck [32]. For example, thresholding methods consider only the image grayscale information, is sensitive to noise, and can lead to uneven segmentation results; the watershed algorithm is prone to over-segmentation due to noise; and graph-theoretical algorithms are complex, computationally intensive, and not user-friendly. Deep learning algorithms are better suited to addressing the challenges of cell segmentation, as they can learn from data and leverage the capabilities of pre-trained models, making them a convenient and effective strategy in many research and application areas [33]. Currently, image processing techniques combined with deep learning have recently seen rapid development in the fields of biology and medicine [34–36]. Liu et al. evaluated 8 cell segmentation tools using three public datasets, including CellProfiler, Icy, StarDist, DeepCell, Cellpose, Omnipose, Plantseg, and Ilastik. They found that Cellpose had best adaptability across different cell types, with noticeable advantages in processing speed and accuracy [33]. Similarly, Han et al. compared DeepCell, Mask R–CNN, and Cellpose, finding that Cellpose could train the best cell segmentation models [37]. However, image processing combined with deep learning in the field of combustion studies, especially in the cell segmentation and feature extraction on the surface of hydrogen-air spherical flames, is still in the preliminary research stage.

Through the literature review above, it becomes clear that fundamental research in combustion science is inseparable from refined and digitalized image processing. Therefore, this paper aims to bridge a gap in the field by concentrating on the integration of image processing techniques with deep learning to analyze the cellular structure characteristics of spherical premixed hydrogen-air flames. The organization of this work is as follows: Firstly, the Cellpose 2.0 graphical user interface (GUI) was innovatively employed in this work for the cell segmentation model training, then a personalized model after training was used to analyze the cellular structures on the surface of spherical flames. Secondly, the related cell information was obtained, such cell number and area. Meanwhile, a new definition of flame radius is proposed, and the flame areas are 3D reconstructed in this work. Finally, the flame stretch rate and flame propagation speed are also derived. The image processing technology based on deep learning and research findings in this work are expected to promote rapid development in the fields of hydrogen explosion safety.

2. Experimental equipment and method

2.1. Optical system arrangement and experimental conditions

As depicted in Fig. 1, the hydrogen-air premixed combustion experiments were carried out in a spherical stainless-steel constant-volume-vessel ((CVV), MK-II) with an internal chamber diameter of 380 mm. However, the maximum observable flame diameter is limited to 150 mm due to the size constraints of the optical windows, which are distributed on the front and back side of CVV. This CVV is designed to withstand initial pressures up to 1.5 MPa and temperatures up to 600 K. Furthermore, after the mixture is introduced into the CVV, it is stirred by four fans driven by 8 kW three-phase motors mounted on the inner walls of the CVV in different orientations, ensuring a uniform mixture of reactants. The combustible premixture inside the CVV is ignited at the center by a spark plug, with a minimal ignition energy of 1 mJ to eliminate any substantial interference during flame propagation. Prior to ignition, the fans are required turned off and the system is allowed to rest for over 15s to ensure complete decay of turbulence and stabilization of the mixture. More detailed experimental information can be
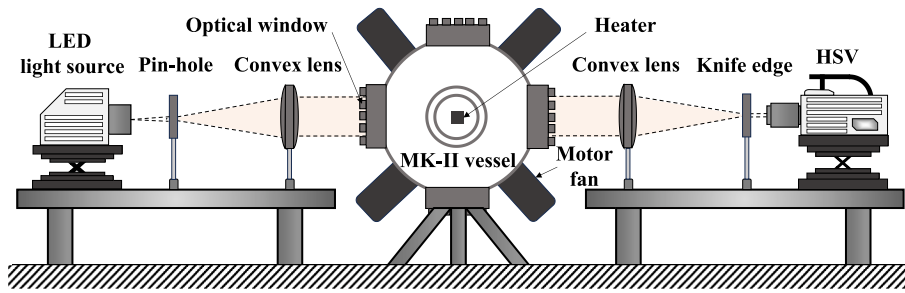
Fig. 1. Schlieren optical diagnostic arrangement.

found in the previous publication [18].

Fig. 1 also presents the high-speed schlieren optical diagnostic arrangement used to measure the morphology and propagation of the spherical hydrogen flame. A light emitting diode (LED) serve as fixed-point light sources and the light expands through a pin-hole onto a convex lens with a focal length of 1 m, creating parallel light that passes through the spherical hydrogen-air flame within the CVV, and is then refocused by another convex lens onto a knife edge. The flame images are captured using a high-speed video (HSV) camera (Phantom v2512, AMETEK) after passing through the knife edge at a frame rate of 10,000 fps and a scale of 0.27 mm/pixel, resulting in 512×512 resolution flame images for post-analysis in this work.

The discussion in this paper is mainly focused on the innovative image processing techniques based on deep learning proposed for the cell structure analysis of spherical flame surfaces. The experimental condition requires the entire process of initial crack appearance, secondary crack formation, and the stable development of cells uniformly covering the flame surface should be fully observed. Therefore, the experimental conditions were unchanged due to the size limitations of the optical window in the CVV, with the initial temperature set to room temperature, the initial ambient pressure at atmospheric pressure, and the fuel-air equivalence ratio (ER) set as 0.8 to observe the complete propagation process of the flame cellularization. Meanwhile, the test was conducted three times under the same condition, and the average is regarded as the final result to ensure the results reliability in this work.

2.2. Deep learning training process and accuracy evaluation

Cellpose is an open-source code on Github that has become a key tool in the field of image analysis, particularly in domains that require detailed cellular examination [38]. Originally developed to address the complexities of biological imaging, Cellpose has played a significant role

in tracking cell growth, morphological changes, and dynamic cellular processes within a biological context [34]. In the field of combustion science, the application of Cellpose introduces a novel concept for flame image processing. Especially in the study of flame instabilities and propagation, algorithms based on deep learning are expected to achieve more precise cell segmentation results. The Cellpose 2.0 GUI, introduced in an article published in nature methods in December 2022 [35], is used in this study to train the cell segmentation model.

Fig. 2 displays the core U-net structure used for convolutional neural network (CNN) model training within Cellpose 2.0 GUI. CNN are a class of deep learning algorithms particularly adept at processing visual data. They function by automatically extracting and learning features from images, which is pivotal in identifying and analyzing cellular characteristics in our context. The U-net architecture, a variant of CNN, is specifically tailored for image segmentation tasks. It features a unique 'U-shaped' design, consisting of two main pathways: a contracting path to capture contextual information and an expansive path that aids in precise localization of cellular boundaries. This dual-pathway structure is highly effective for detailed image segmentation, a critical aspect in cellular analysis. Here, the convolutional kernel, with its size of 3×3, acts as a small window sliding across the image to capture and analyze local features like edges and textures. This size is a strategic choice, balancing the need for detail capture and computational efficiency. Meanwhile, the maximum pooling layer, with a 2×2 window size, plays a crucial role in this architecture. Pooling is a process that reduces the size of the feature maps by summarizing regions, thus decreasing the computational load and the risk of overfitting. The 2×2 size is specifically chosen to effectively downsize the image representations while retaining the most relevant features, aiding in the efficient and accurate segmentation of cells. Further enhancing the functionality of U-net within Cellpose are the inclusion of residual blocks and skip connections. Residual blocks facilitate the learning process by enabling the
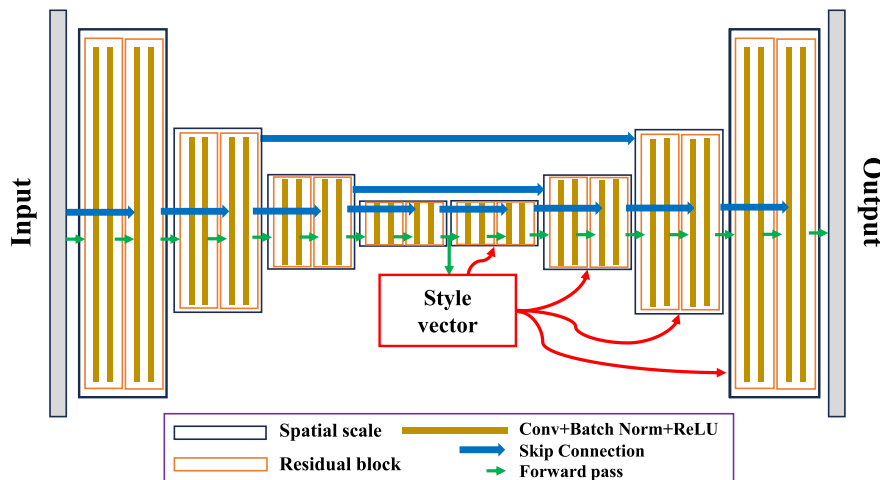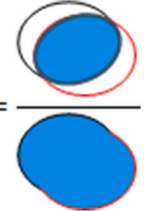

Fig. 2. U-net architecture used in Cellpose 2.0 [35].

network to identify more complex patterns, while skip connections help in preserving spatial information during the segmentation process. These features collectively ensure that the final model achieves high accuracy in delineating cell boundaries, which is of paramount importance in both biological and combustion science research.

Fig. 3 can be used to guide users to employ the Cellpose 2.0 GUI for training personalized models, anchored in the core concept of an "interactive machine learning loop" between human and machine, which is also an upgrade compared to Cellpose 1.0. The study in Nature Methods showed that they have trained numerous different types of cells and used the Leiden algorithm to classify them into nine clusters named CP, TN1, TN2, TN3, LC1, LC2, LC3, LC4, and CPx, collectively known as the "model zoo", greatly improving the model training efficiency for subsequent researchers [35]. In this work, the interactive approach begins with a model selected from "model zoo". The human-in-the-loop involves human intervention as follows: (1) The process starts by selecting a model from the "model zoo" and setting an assumed cell diameter to initiate training; (2) A new flame image is imported; (3) Initially, the results may be suboptimal, or even poor, necessitating human intervention to manually add region of interests (ROIs) that are believed to represent cells; (4) After this intervention, the model is trained again, building upon the previous iteration to develop a personalized model; (5) Through several cycles of this process, when the number of manually added ROIs approaches zero, a personalized model is considered trained for segmenting and identifying cellular structures in flame images. However, due to inherent limitations of flame imagery and the distinct growth processes compared to biological cell images, achieving a manual ROI count of zero may not be feasible. In fact, it should be mentioned that it spends amount of time to select different initial models from "model zoo" to train the cellularized flame images and compare the effect, finally determining that "CPx" as the initial model with the best effect. Future work could directly utilize the pre-trained cell segmentation model in this work to train other spherical cellularized flame images, thereby significantly improving training efficiency in the field of combustion. Subsequently, a commonly used metric intersection over union (IoU) and average precision (AP) will be utilized to evaluate the training process of the personalized model trained in this paper [39].

IoU serves as a pivotal metric for evaluating the accuracy of segmentation models as they pertain to the cellular structures on flame surfaces. When a model predicts the boundary of a cell on a flame surface, IoU assesses the accuracy by measuring the overlap between the predicted cell boundary (B_{pred}, represented by the black outline ellipse in Equation (1)) and the true cell boundary (B_{gt}, represented by the red outline ellipse in Equation (1)). Then, the IoU can be calculated from Equation (1). An IoU score close to 1 indicates a high degree of accuracy, with the predicted cell boundary almost exactly matching the true cell boundary. Conversely, an IoU score approaching 0 signifies poor model performance with little to no overlap between the predicted and true boundaries.

$$IoU = \frac{Area\ of\ Overlap}{Area\ of\ Union} = \frac{B_{pred} \cap B_{gt}}{B_{pred} \cup B_{gt}} = \qquad (1)$$

AP in the context of flame surface cell segmentation is a comprehensive metric that takes into account the precision and recall across a range of IoU thresholds. For each IoU threshold, a detection is considered a true positive if the IoU between the predicted cell boundary and the ground truth is above that threshold, reflecting accurate segmentation. To calculate AP, a set of IoU thresholds, typically between 0.5 and 0.95 at an increment of 0.05, will be established first. At each threshold, precision (the proportion of true positive detections out of all positive detections) and recall (the proportion of true positive detections out of all actual cells on the flame surface) are calculated. AP is then the average of the precision values at each IoU level, weighted by the increase in recall relative to the previous IoU threshold. Equation (2) now explicitly reflects this relationship:

$$AP = \sum (C_n - C_{n-1}) \times P_n (IoU_{threshold}) \qquad (2)$$

Here, $P_n (IoU_{threshold})$ is the precision at a given IoU threshold and C_n is the recall at that threshold. The summation runs across all IoU thresholds.

This relationship between AP and IoU thresholds showcases how the model performs not just at one level of segmentation accuracy, but across a spectrum. A high AP indicates that the model not only segments cells accurately at a basic level of overlap (a low IoU threshold) but also maintains high precision at stricter levels of accuracy (higher IoU thresholds), which is crucial for detailed analysis of flame surface cells where precision in boundary detection can be critical. Leveraging
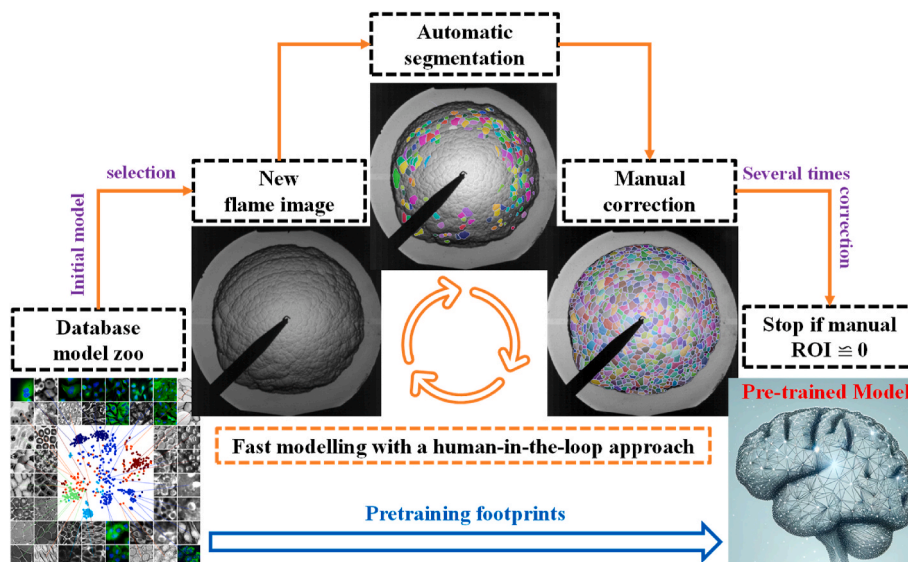

Fig. 3. Cell segmentation model pretraining process using Cellpose 2.0 GUI.

insights from above relationship, a novel program specifically designed to compute the AP for image segmentation has been developed. As observed in Fig. 4 (a), the initial stage 1 of training, which precedes the emergence of small-scale cells, yields an AP of 0.575. In the subsequent stage 2, marked by the presence of numerous small-scale cells, the AP experiences a notable increase to approximately 0.625. Further increments in the number of training images do not substantially alter this value, indicating a plateau likely due to the inherent quality constraints of flame images. Remarkably, a training set of no more than 20 images suffices, thereby significantly enhancing the model training efficiency. Moreover, the trend depicted in Fig. 4 (b) showcases that with an increase in manually added ROIs, there is a swift augmentation in AP following the first training iteration, which then rapidly stabilizes. However, it is not accurate to conclude that the number of manually added ROIs will progressively decrease due to the dynamic nature of cell division, with variations in cell shape, size, and quantity continuously unfolding. Focusing solely on the AP value itself is therefore more pertinent. As pointed in the publication [37], the segmentation accuracy for most biological cells reaches an AP about 0.7. Through the tailored training for flame imagery in this work, an AP of 0.625 for cell segmentation has been achieved, which can be considered the most effective cell recognition method currently in the field of combustion.

2.3. Comprehensive image processing process

As illustrated in Fig. 5, a comprehensive workflow for image processing is presented following the successful training of the cell segmentation model in Section 2.2. The initial step involves a series of preprocessing techniques applied to the flame images, which primarily includes background subtraction, brightness enhancement, contrast amplification, noise reduction, and automatic thresholding via Otsu's method. The binary image resulting from these operations is then further processed by employing morphological closing operations to address the distortions caused by the ignition device, which facilitate the capture of large-scale flame contours. The derived flame contours are then superimposed onto the original image using green lines.

Subsequently, the trained cell segmentation model from Section 2.2 is integrated to delineate the boundaries of small-scale cells. Within the processed image, the centroids of each small-scale cell are identified and labeled. These image processing steps above yields quantitative data, including the count of small-scale cells, their centroid positions, perimeters, areas, and average area. In addition, large-scale flame features, such as the flame boundary, equivalent flame radius, and the total length of contours, also be extracted, thereby providing a rich dataset for subsequent analysis. In order to accurately calculate the flame radius, it

is noteworthy that the region obscured by the ignition device, indicated by the angle between the two yellow lines, is excluded from post-processing considerations, accounting for 7.5% of the total angular proportion (the angle measured by image processing is 27°). For the detailed video demonstration of the comprehensive image processing process, please refer to the PowerPoint in the Supplementary Material part.

2.4. 3D reconstruction of small-scale cells

The 2D flame images obtained via schlieren technique lost the depth and complexity of the flame structure. The corresponding author of this article is the first one to propose that 3D mapping can be used to reconstruct the true flame morphology [26]. As illustrated in Fig. 6, Xu et al. provided a detailed derivation of the 3D reconstruction process for the 2D cell area [27]. Herein, the centroid O of the 2D flame image is regarded as the origin of the coordinate system, and $P(x,y,z)$ denotes a point on the surface of a 3D sphere characterized by an equivalent flame radius r_u, which also represents the mapping of a point within an enclosed cell region D onto the spherical surface. The coordinates of the mapping point $P(x,y,z)$ on the 3D spherical surface for any point within the enclosed cell region D can be ascertained using Equation (3).

$$z^2 = r_u^2 - x^2 - y^2 \tag{3}$$

Furthermore, the cosine of the angle γ between the tangent plane at mapping point $P(x,y,z)$ on the sphere and the projection plane of $P(x,y,z)$ can be calculated using Equation (4):

$$\cos \gamma = \frac{1}{\sqrt{1 + \left(\frac{\partial z}{\partial x}\right)^2 + \left(\frac{\partial z}{\partial y}\right)^2}} \tag{4}$$

When the pixels in the enclosed cell region D are small enough, $d\varsigma = dAp \cos \gamma$. dAp is the actual mapping area of the projection pixels in the enclosed cell region and $d\varsigma$ is the projection pixels area, respectively. Thus, the actual cell area A corresponding to the enclosed cell region D on the 2D projection plane can be calculated as Equation (5):

$$A = \sum_D \sqrt{1 + \left(\frac{\partial z}{\partial x}\right)^2 + \left(\frac{\partial z}{\partial y}\right)^2} \, d\varsigma \tag{5}$$

2.5. Uncertainty analysis

The subsequent results of this work focus on discussing the effectiveness the deep learning-trained cell segmentation model on the
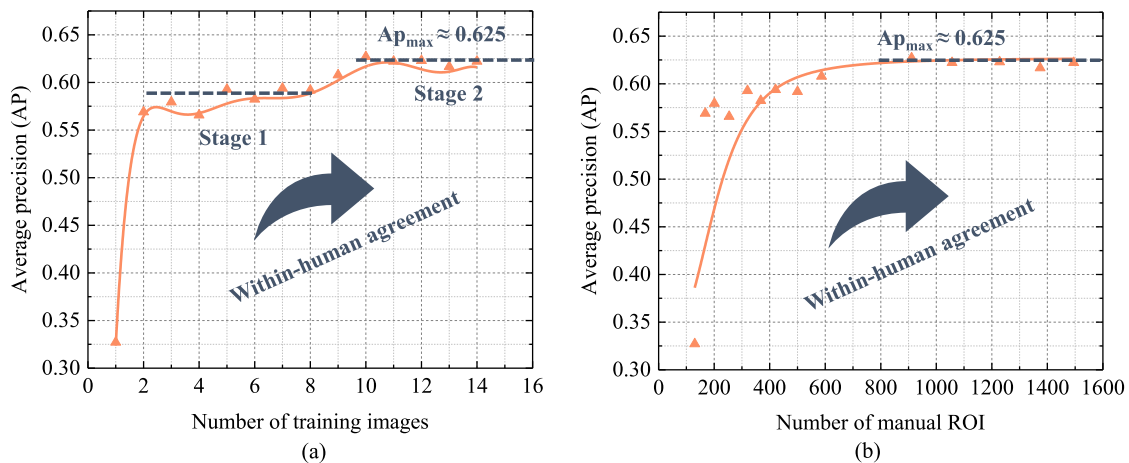

Fig. 4. Average precision (AP) evaluation during the model online pretraining process.
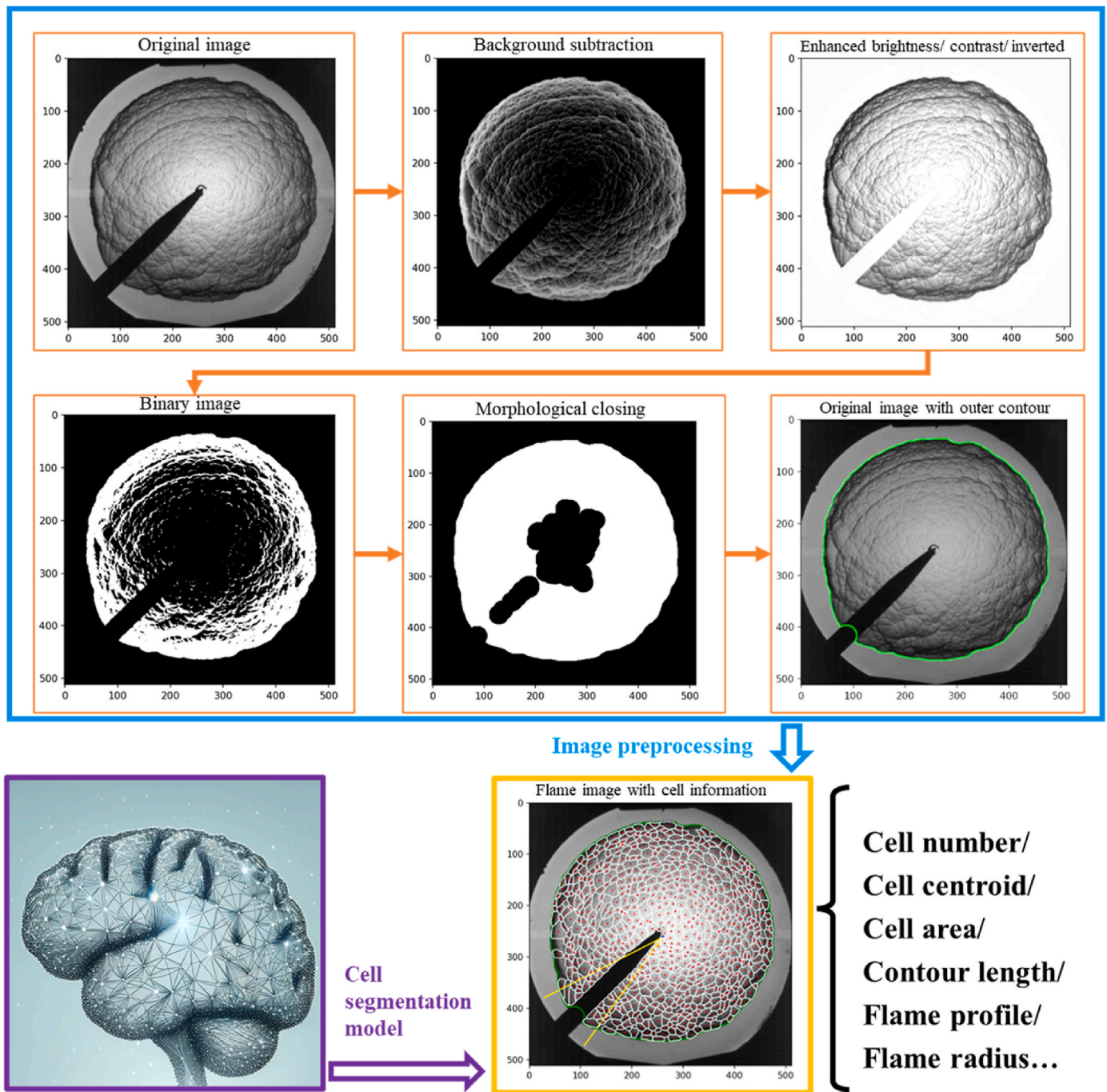
Fig. 5. Image processing process for small-scale cell and large-scale flame features.

results of image processing. As shown in Fig. 4, the AP is used to describe the accuracy of the model, and an AP value of 0.625 is considered to achieve a good segmentation effect [35,37]. Due to the limitations of the experimental equipment, the captured flame images are affected by the ignition device. The uncertainty in algorithm quantification during the image processing is mainly due to the region affected by the ignition device, which accounts for approximately 7.5% of the entire image (this is converted from the coordinate angle of 27° obtained during the image processing). Furthermore, as known from the 3D-reconstruction work from Xu et al., the error in the 3D reconstruction algorithm of the cell area is about 3.97% [27]. These uncertainties mentioned above can be considered as quantifiable uncertainties in this work.

3. Results and discussion

3.1. Evolution of the hydrogen-air spherical flame

Fig. 7 shows the evolution of the morphology of hydrogen-air pre-mixed flames at ER0.8. It is observed that large cracks appear in the early stages, which could be attributed to the uneven distribution of spark ignition energy and the heterogeneity of the unburned mixture locally [40]. It also can be seen that at $T = 4$ ms into flame propagation, the entire flame surface is covered with numerous small-scale cells. The emergence of these small-scale cells is primarily due to the coupling of thermal diffusion instability and hydrodynamic instability, buoyancy instability can be neglected in this study due to the overall spatial scale limitation [11].
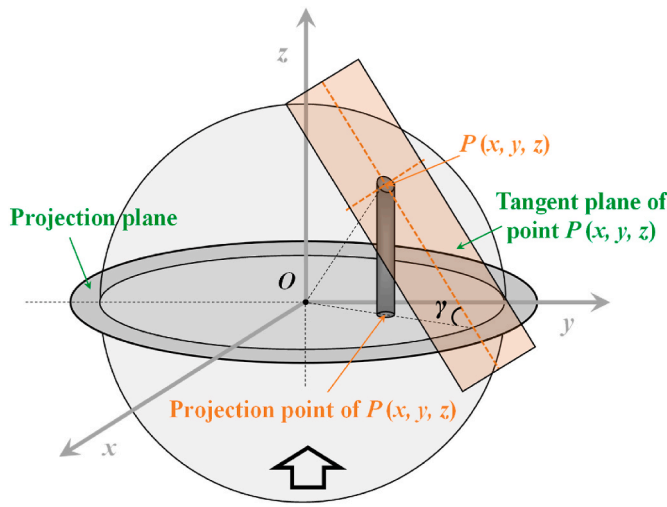
Fig. 6. Three-dimensional reconstruction of small-scale cell.

3.2. Flame profiles and flame radius

In this work, the equivalent flame radius r_u is defined as the average distance from the flame centroid to those points on the flame profile. Fig. 8 (a) and (b) captures the flame profiles and the flame radius growth

trend over time. As time progresses, it is noted that the fluctuations in the flame profiles are gradually amplified. The flame radius consistently expands, ultimately reaching a maximum of approximately 62 mm due to the constraints of the CVV optical window [18]. In the initial phase of flame propagation, ignition energy significantly influences the flame front, especially when the flame radius is small. The ignition energy heats and ignites the adjacent combustible mixture, forming an unstable initial flame kernel that is sensitive to environmental disturbances [41]. As the flame expands, its interaction with the combustion chamber walls becomes significant. Wall confinement affects the flame through thermal conduction, reflection, and cooling, altering the flame shape and combustion efficiency [42]. As shown in Fig. 8 (b), a light red mask covers the early effects of ignition energy, while a light blue mask obscures the impact of later wall confinement. According to the definition of the three onset described by Zhao et al., R_{C1}, R_{C2} and R_{C3} represent the critical flame radius of crack branching, uniform cellularity and transition acceleration, respectively. Specifically, it is found that the transition acceleration occurs slightly later than crack branching while the uniform cellularity appears far later than the former two onsets [12]. The results identified the critical flame radius R_{C1} and R_{C3} are approximately 29.77 mm and 53.88 mm, respectively, which are observed in the raw flame images. The onset of transition acceleration R_{C2} will be derived in the next section. Moreover, the flame radius and critical flame radius data provides a critical foundation for subsequent analysis of other parameters.
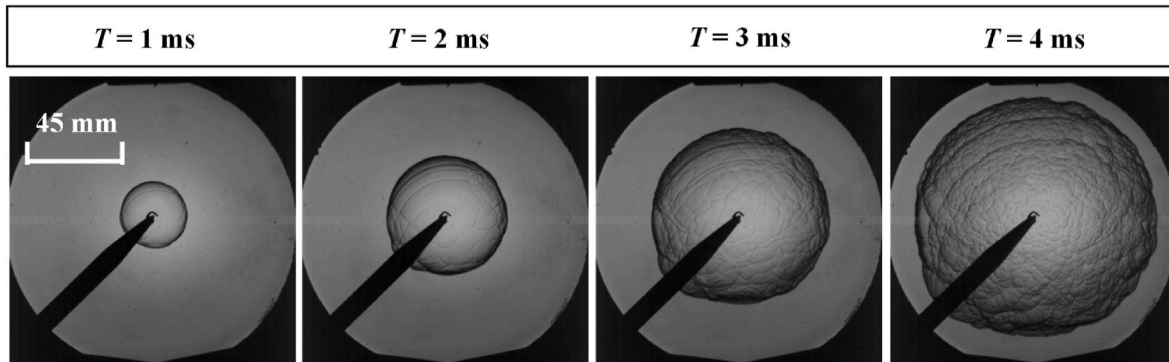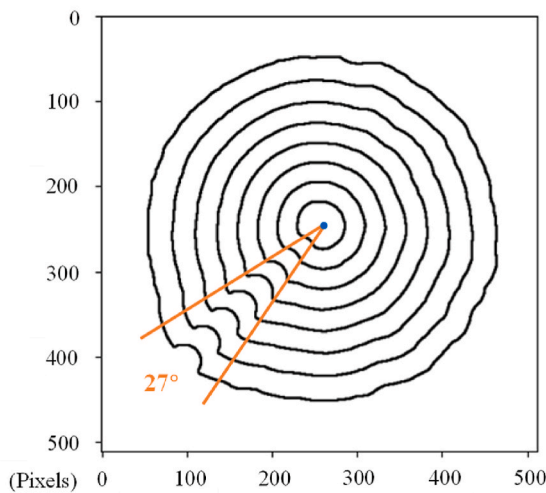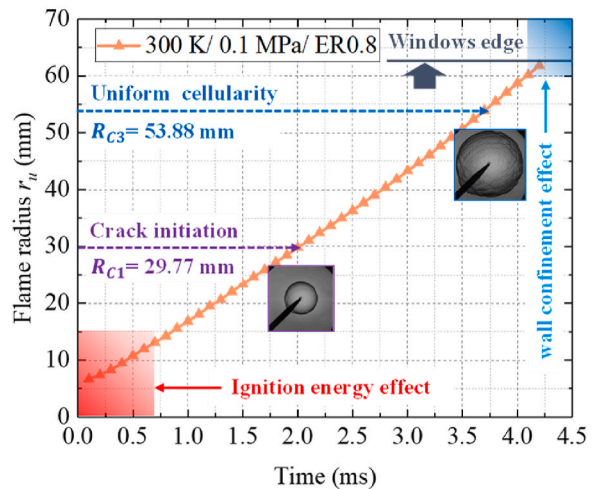

Fig. 7. Evolution of hydrogen-air premixed flame morphology [300 K/0.1 MPa/ER0.8].

(a) Flame profiles

(b) Flame radius

Fig. 8. Evolution of flame profiles and flame radius r_u.

3.3. Flame stretch rate and propagation speed

The flame stretch rate significantly affects the flame propagation speed and limits the development of disturbances at the flame front, thereby influencing the evolution of the flame cellular structure. The flame stretch rate, κ, is defined as [43]:

$$\kappa = \frac{1}{A_f}\frac{dA_f}{dt} = \frac{2}{r_u}\frac{dr_u}{dt} = \frac{2}{r_u}S_n \qquad (6)$$

where A_f is the surface area of the laminar flame. The stretched flame speed, S_n, is calculated based on the evolution of the equivalent flame radius r_u over time ($S_n = dr_u/dt$).

As shown in Equation (6), the flame propagation speed S_n has a relationship with the flame stretch rate κ [44]. Equation (7) can be used to calculate the unstretched flame propagation speed S_L, and the selected flame images for calculation should avoid the influence of ignition energy, inherent flame instability, and pressure.

$$S_L - S_n = L_b\kappa \qquad (7)$$

where S_L can be obtained by linear extrapolating S_n to zero stretch rate, and L_b is the Markstein length of the burnt gas.

Fig. 9 (a) demonstrates the variation in flame stretch rate κ relative to flame radius r_u. A higher stretch rate κ typically signifies a propensity towards instability in the flame. The results indicate a noticeable decline in the stretch rate κ concurrent with the increase in flame radius. This global trend might be attributed to the spherical flames transition to a "quasi-saturation state", characterized by a balanced state of competitive relationship between flame propagation and cell division [30].

Fig. 9 (b) provides a comprehensive analysis of stretched flame speed S_n in relation to the stretch rate κ. Due to the irregularities in the early stages of flame propagation, likely influenced by ignition, the velocities within the light pink shaded area are deemed erratic and thus are not considered for this flame speed analysis. The results demonstrate that the initial stretch flame speed is essentially linear, extrapolating linearly to a stretch rate of zero yields an unstretched flame propagation speed S_L of 12.4 m/s. Additionally, the onset of transition acceleration R_{C2} can be derived from the green arrow line Fig. 9 is about 36 mm. Furthermore, once the flame propagation exceeds this transition acceleration critical radius R_{C2}, the stretch flame speed exhibits a self-accelerating trend.

3.4. Basic cell number and total crack length

Fig. 10 (a) illustrates the cell numbers N as a function of with the flame radius r_u, obtained through meticulous image processing based on

deep learning. Meanwhile, the three onsets of critical flame radius identified are indicated in this Figure as well. In this study, a correction to the cell number data were implemented. To compensate for the loss of cell number information within the region containing the ignition device, we adjusted the total cell count by dividing 0.925, reflecting the proportional 7.5% obscured by the angle of the device. Results show that a general trend of increasing cell number N is observed with the flame propagation, meanwhile, there is a relative increase in the average growth rate of cell number N after each onset. Notably, a marked acceleration can be seen after the transition acceleration critical radius R_{C2}, which can be attributed to a profusion of small-scale cells manifesting on the flame surface. The proliferation of these minuscule cells is known to exacerbate flame instability, precipitating a self-accelerating phenomenon [45]. Fig. 10 (b) illustrates the development of the total contour length L with the flame radius r_u, where the crack length is defined as the sum of the contours of all identified small cells and calculated using in-house image processing procedure. It can be seen that the total contour length L increases continuously with the burgeoning number of cells. When the flame development exceeds the transition acceleration critical radius R_{C2}, an interesting trend of linear crack growth is observed in this work, corroborating that a dynamic equilibrium is attained in the later stages of flame cellularization.

3.5. Cell area statistic distribution and average cell area

Utilizing the cell area 3D reconstruction concept introduced in Section 2.4, Fig. 11 (a) and (b) provides the statistical distribution of flame cell areas, using probability density function (PDF), on the flame surface before and after 3D reconstruction at $T = 3$ ms and $T = 4.2$ ms (the timing when flame approach to the optical window edge), respectively. The analysis reveals that when comparing the cell distributions before and after 3D reconstruction, the cell number is the same, and a common point is that the cell areas distribution is concentrated in small cell areas. Meanwhile, comparing Fig. 11 (a) and (b), it is found that the cell area will become more concentrated towards smaller values over time. Additionally, the statistical distribution of cell area after 3D reconstruction is clearly shifted towards larger values. This shift could be attributed to the added depth dimension, which unveils the true extent of the cell sizes that the 2D projection underestimates.

Fig. 12 delineate the progression of average cell area in both 2D and 3D reconstructions as the flame radius r_u develops. It is observed that the average cell area was increased after 3D reconstruction compared to 2D average cell area. When the spherical flame development exceeds the transition acceleration critical radius R_{C2}, the change in 2D & 3D average cell area shows a rapidly declining trend, which can be
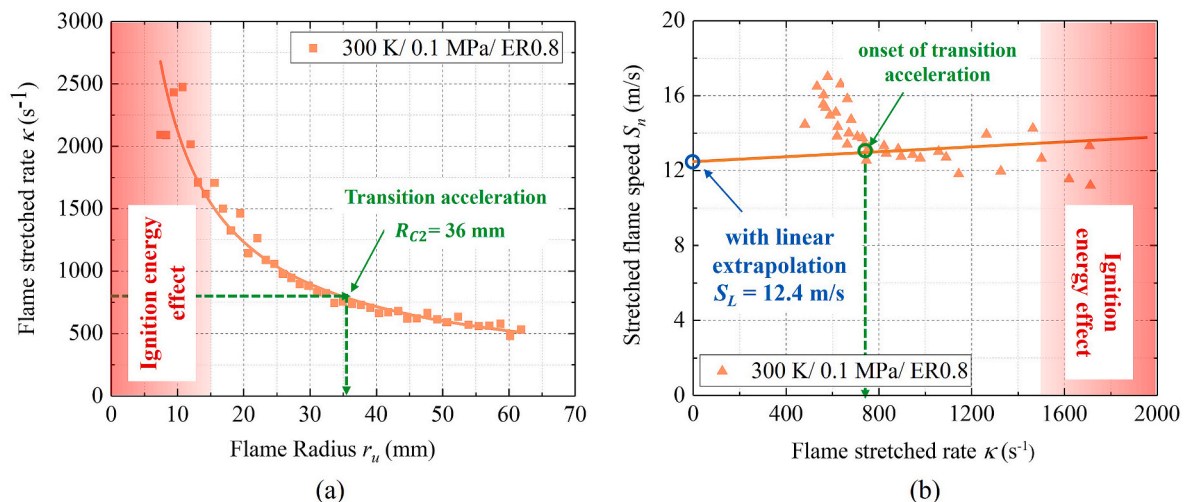
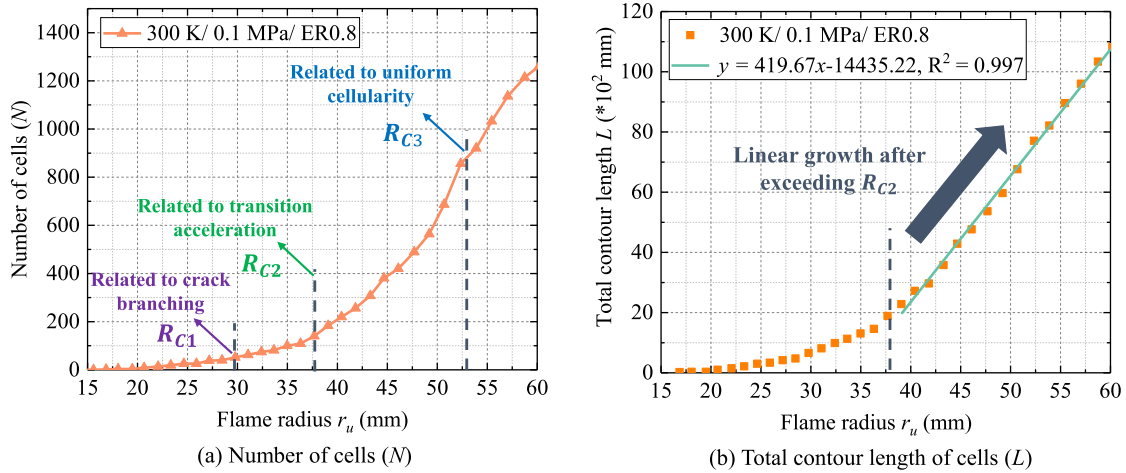**Fig. 9.** Development of flame stretched rate κ and stretched flame speed S_n.

(a) Number of cells (N)

(b) Total contour length of cells (L)

Fig. 10. Development of cells number (N) and crack length (L) with flame radius r_u.

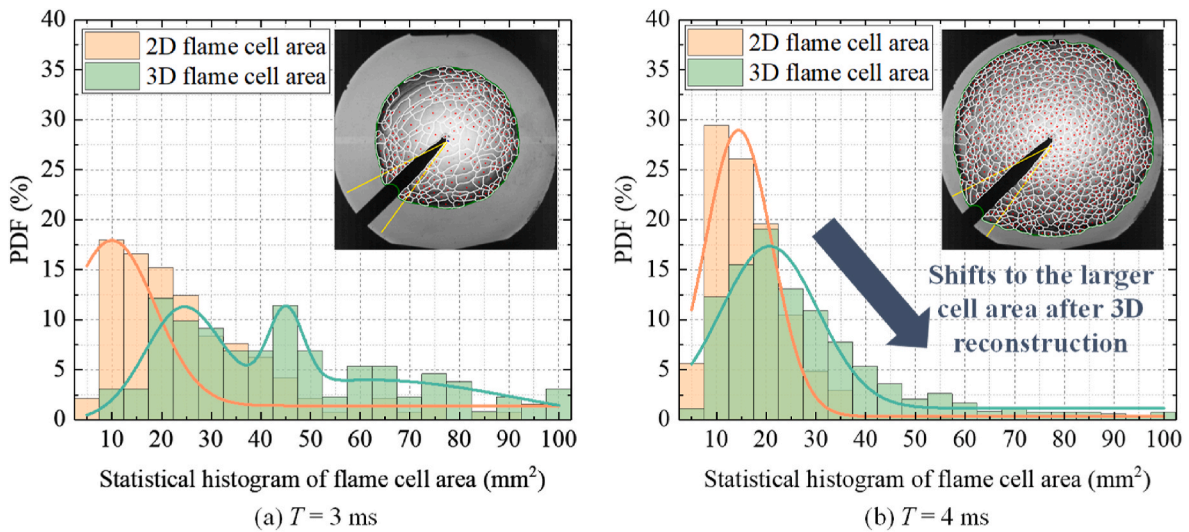(a) $T = 3$ ms

(b) $T = 4$ ms

Fig. 11. Statistical distribution of cell area before and after 3D reconstruction.
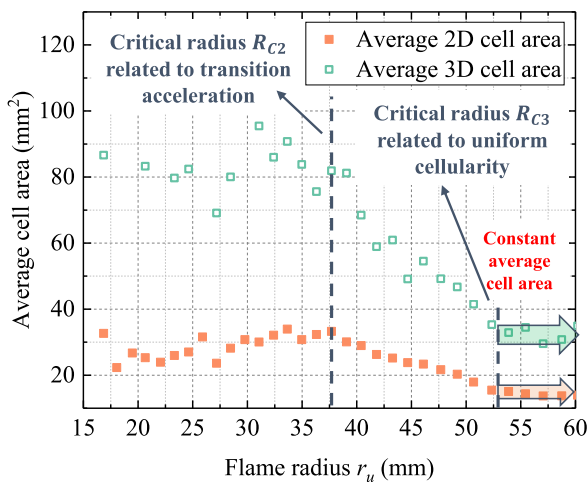

Fig. 12. Development of 2D & 3D average cell area with flame radius r_u.

attributed to the rapid increase in the cells number of flame surface. Ultimately, the average cell area tends towards a relatively stable value after the flame radius exceeds the uniform cellularity critical radius R_{C3}, at which point the flame cellularization can be considered to have reached a state of dynamic equilibrium. Specially, once the spherical flame surface becomes uniformly covered with small-scale cells, the 2D cell area stabilizes at an approximate value of 14 mm^2, corresponding to an average 2D cell diameter of about 4.22 mm. Meanwhile, the 3D average cell area gradually converges to a steady value of approximately 32 mm^2 at last.

4. Conclusions

The propagation speed of spherical flames is closely related to the cellular structures on their surfaces. Investigating these cellular structures on the surface of spherical flames is of great importance, especially in scenarios involving explosions. In this work, high-speed schlieren optical diagnostic techniques were used to obtain the spherical flames images. Then, advanced image processing technologies driven by deep learning were developed to perform a detailed analysis of the cellular structure characteristics of spherical premixed hydrogen-air flames. The specific research results are as follows.

(1) The average precision (AP) of the cell segmentation model pre-trained using Cellpose 2.0 for the spherical flame surface reached 0.625. This level of precision enables effective cell segmentation.

(2) The flame radius continuously expands with time going. Additionally, the stretch rate significantly decreases with increasing flame radius, which can be attributed to the flame transition to a "quasi-saturation state" of dynamic equilibrium.

(3) The obtained un-stretched flame speed is 12.4 m/s under an equivalent ratio of 0.8. Meanwhile, the critical flame radius R_{C2} of transition acceleration obtained is 36 mm. Eventually, the flame propagation exhibits a self-accelerating trend once it exceeds this critical radius.

(4) The number of cells shows an overall increasing trend over time, with acceleration particularly evident in the later stages, which can be attributed to a profusion of small-scale cells manifesting on the flame surface. Meanwhile, the total cell contour length continuously increases with the number of cells. Interestingly, the growth of the crack length shows a linear trend after the flame development exceeds the critical flame radius R_{C2} of transition acceleration.

(5) Owing to the increase in cell area in the depth dimension, the distribution of cell areas after three-dimensional reconstruction shifts towards larger value. Concurrently, the average cell area gradually converges to a stable value due to the balance of competitive relationship between flame propagation and cell division after the flame radius exceeds uniform cellularity critical radius R_{C3}.

Future work

Extensive training to adapt to the recognition and segmentation of cellular structures on the surface of spherical flames under a wide range of experimental conditions will further improve the precision of the deep learning model in terms of cell feature extraction, such as the various initial temperature, pressure, low equivalence ratio conditions, and other premixed fuels. The cell segmentation model pre-trained in this work is placed in the Github (http://tinyurl.com/yt2ysvah) for further training and use by researchers in the field of combustion. After we fully develop the proposed deep learning model for cell extraction, we will move to new tools, such as DeepCell and Mask R–CNN, to train cell segmentation models and perform segmentation tests and comparison.

Declaration of competing interest

The authors declare that they have no known competing financial interests or personal relationships that could have appeared to influence the work reported in this paper.

Appendix A. Supplementary data

Supplementary data to this article can be found online at https://doi.org/10.1016/j.ijhydene.2024.04.232.

Nomenclature

2D	two-dimensional
3D	three-dimensional
CVV	constant volume vessel
ER	equivalence ratios
LED	light emitting diode
HSV	GUI high-speed video camera graphical user interface
CNN	convolutional neural network
ROIs	region of interests
IoU	intersection over union
AP	average precision
B_{pred}	predicted cell boundary
B_{gt}	true cell boundary
$P_n\,(IoU_{threshold})$	precision at a given IoU threshold
C_n	recall at a same IoU threshold
O	flame centroid (origin)
r_u	equivalent flame radius
γ	angle between the tangent plane and the projection plane
D	enclosed cell region
A	actual 3D cell area
N	cell number
T	time after ignition
L	contour length
R_{C1}	critical flame radius of crack branching
R_{C2}	critical flame radius of uniform cellularity
R_{C3}	critical flame radius of transition acceleration
κ	flame stretch rate
S_n	laminar stretch flame speed
S_L	unstretched flame speed
L_b	Markstein length
A_f	surface area of the laminar flame

References

[1] IEA. The future of hydrogen. Paris, https://www.iea.org/reports/the-future-of-hydrogen,License:CCBY4.0. [Accessed 10 January 2024].

[2] Jin Y, Luo H, Zhang G, Zhai C, Ogata Y, Matsumura Y, et al. Ignition timing effect on the combustion performance of hydrogen addition in methane fermentation gas in a local energy system. Fuel 2022;324:124714. https://doi.org/10.1016/j.fuel.2022.124714.

[3] Chen P, Shen Ta, Xie Y, Su X. Initial flame propagation characteristics of the hydrogen spherical premixed flame. Int J Hydrogen Energy 2023;48:36112–21. https://doi.org/10.1016/j.ijhydene.2023.05.348.

[4] Cai X, Wang J, Zhao H, Zhang M, Huang Z. Flame morphology and self-acceleration of syngas spherically expanding flames. Int J Hydrogen Energy 2018;43:17531–41. https://doi.org/10.1016/j.ijhydene.2018.07.140.

[5] Liu C, Tang K, Huang C, Liu J, Liu L. Effect of initial pressure on the critical characteristics and overpressure of hydrogen-air premixed gas combustion and explosion. Int J Hydrogen Energy 2024;49:311–22. https://doi.org/10.1016/j.ijhydene.2023.07.266.

[6] Xie Y, Wang X, Bi H, Yuan Y, Wang J, Huang Z, et al. A comprehensive review on laminar spherically premixed flame propagation of syngas. Fuel Process Technol 2018;181:97–114. https://doi.org/10.1016/j.fuproc.2018.09.016.

[7] Oppong F, Luo Z, Li X, Song Y, Xu C. Intrinsic instability of different fuels spherically expanding flames: a review. Fuel Process Technol 2022;234:107325. https://doi.org/10.1016/j.fuproc.2022.107325.

[8] Li Y, Xu W, Jiang Y, Liew KM. Effects of diluents on laminar burning velocity and cellular instability of 2-methyltetrahydrofuran-air flames. Fuel 2022;308:121974. https://doi.org/10.1016/j.fuel.2021.121974.

[9] Yin L, Xu W, Hu Y, Jiang Y. Experimental and theoretical investigation of ethyl methyl carbonate/air flames: laminar burning velocity and cellular instability at elevated pressures. Fuel 2023;346:128206. https://doi.org/10.1016/j.fuel.2023.128206.

[10] Wu F, Jomaas G, Law CK. An experimental investigation on self-acceleration of cellular spherical flames. Proc Combust Inst 2013;34:937–45. https://doi.org/10.1016/j.proci.2012.05.068.

[11] Yang S, Saha A, Wu F, Law CK. Morphology and self-acceleration of expanding laminar flames with flame-front cellular instabilities. Combust Flame 2016;171:112–8. https://doi.org/10.1016/j.combustflame.2016.05.017.

[12] Zhao H, Wang J, Bian Z, Cai X, Li X, Huang Z. Onset of cellular instability and self-acceleration propagation of syngas spherically expanding flames at elevated pressures. Int J Hydrogen Energy 2019;44:27995–8006. https://doi.org/10.1016/j.ijhydene.2019.09.038.

[13] Beeckmann J, Hesse R, Kruse S, Berens A, Peters N, Pitsch H, et al. Propagation speed and stability of spherically expanding hydrogen/air flames: experimental study and asymptotics. Proc Combust Inst 2017;36:1531–8. https://doi.org/10.1016/j.proci.2016.06.194.

[14] Cai X, Wang J, Bian Z, Zhao H, Dai H, Huang Z. On transition to self-similar acceleration of spherically expanding flames with cellular instabilities. Combust Flame 2020;215:364–75. https://doi.org/10.1016/j.combustflame.2020.02.001.

[15] Kim W, Imamura T, Mogi T, Dobashi R. Experimental investigation on the onset of cellular instabilities and acceleration of expanding spherical flames. Int J Hydrogen Energy 2017;42:14821–8. https://doi.org/10.1016/j.ijhydene.2017.04.068.

[16] Kim W, Sato Y, Johzaki T, Endo T. Experimental study on the onset of flame acceleration due to cellular instabilities. J Loss Prev Process Ind 2019;60:264–8. https://doi.org/10.1016/j.jlp.2019.05.008.

[17] Kim W, Namba T, Johzaki T, Endo T. Self-similar propagation of spherically expanding flames in lean hydrogen–air mixtures. Int J Hydrogen Energy 2020;45:25608–14. https://doi.org/10.1016/j.ijhydene.2020.06.261.

[18] Xie Y, Elsayed Morsy M, Li J, Yang J. Intrinsic cellular instabilities of hydrogen laminar outwardly propagating spherical flames. Fuel 2022;327:125149. https://doi.org/10.1016/j.fuel.2022.125149.

[19] Zhao H, Wang J, Cai X, Dai H, Liu X, Li G, et al. On accelerative propagation of premixed hydrogen/air laminar and turbulent expanding flames. Energy 2023;283:129106. https://doi.org/10.1016/j.energy.2023.129106.

[20] Han Z, Xiao B, Tian W, Li J, Yu W. Study on difference and adaptability of calculation method of spherical flame radius. Fuel 2020;259:116216. https://doi.org/10.1016/j.fuel.2019.116216.

[21] Sun Z. Structure of turbulent rich hydrogen-air premixed flames. Int J Energy Res 2018;42:2845–58. https://doi.org/10.1002/er.4048.

[22] Zhang G, Li G, Li H, Lv J. Experimental study of the flame structural characteristics and self-similar propagation of syngas and air turbulent expanding premixed flame. J Energy Eng 2021;147:04020090. https://doi.org/10.1061/(ASCE)EY.1943-7897.0000742.

[23] Jiang Y, Li G, Li H, Li L, Zhang G. Effect of flame inherent instabilities on the flame geometric structure characteristics based on wavelet transform. Int J Hydrogen Energy 2018;43:9022–35. https://doi.org/10.1016/j.ijhydene.2018.03.141.

[24] Wu H, Zheng J, Dong X, Zhang S, Ding Y. Investigations on the cellular instabilities of expanding hydrogen/methanol spherical flame. Int J Hydrogen Energy 2021;46:33601–15. https://doi.org/10.1016/j.ijhydene.2021.07.194.

[25] Jiang Y, Li G, Li F, Sun Z, Li H. Experimental investigation of correlation between cellular structure of the flame front and pressure. Fuel 2017;199:65–75. https://doi.org/10.1016/j.fuel.2017.02.036.

[26] Xu HM. Key findings in 'MF and DMF - engine performance'. https://www.birmingham.ac.uk/research/activity/mechanical-engineering/case-centre/vehicle-technology/future-power/mf-and-dmf-engine-performance/key-findings.aspx. [Accessed 10 January 2024].

[27] Li X, Wang Q, Oppong F, Liu W, Xu C. Cellularization characteristics of ethyl acetate spherical expanding flame. Fuel 2021;291:120213. https://doi.org/10.1016/j.fuel.2021.120213.

[28] Xu C, Wang Q, Li X, Oppong F, Liu W. The effect of intrinsic instability on the surface topography of spherical 2-acetylfuran flame. Fuel 2022;318:123624. https://doi.org/10.1016/j.fuel.2022.123624.

[29] Xu C, Liu W, Oppong F, Wang Q, Sun Z-Y, Li X. Investigations on cellularization instability of 2-ethylfuran. Renew Energy 2022;191:447–58. https://doi.org/10.1016/j.renene.2022.04.068.

[30] Bao Y, Li X, Xu C, Wang Q, Oppong F. Experimental and theoretical study of 2-ethylfuran spherical expanding flame: cellularization, intrinsic instability and self-acceleration. Fuel Process Technol 2022;238:107521. https://doi.org/10.1016/j.fuproc.2022.107521.

[31] Xu C, Bao Y, Li X, Qian L, Oppong F. Pressure fluctuation and cellularization characteristics of 2-ethylfuran spherical expanding flame. Fuel 2023;349:128627. https://doi.org/10.1016/j.fuel.2023.128627.

[32] Scherr T, Seiffarth J, Wollenhaupt B, Neumann O, Schilling MP, Kohlheyer D, et al. microbeSEG: a deep learning software tool with OMERO data management for efficient and accurate cell segmentation. PLoS One 2022;17:e0277601. https://doi.org/10.1371/journal.pone.0277601.

[33] Liu P, Li J, Chang J, Hu P, Sun Y, Jiang Y, et al. Software tools for 2D cell segmentation. Cells 2024;13. https://doi.org/10.3390/cells13040352.

[34] Stringer C, Wang T, Michaelos M, Pachitariu M. Cellpose: a generalist algorithm for cellular segmentation. Nat Methods 2021;18:100–6. https://doi.org/10.1038/s41592-020-01018-x.

[35] Pachitariu M, Stringer C. Cellpose 2.0: how to train your own model. Nat Methods 2022;19:1634–41. https://doi.org/10.1038/s41592-022-01663-4.

[36] Maška M, Ulman V, Delgado-Rodriguez P, Gómez-de-Mariscal E, Nečasová T, Guerrero Peña FA, et al. The cell tracking challenge: 10 years of objective benchmarking. Nat Methods 2023;20:1010–20. https://doi.org/10.1038/s41592-023-01879-y.

[37] Han S, Phasouk K, Zhu J, Fong Y. Optimizing deep learning-based segmentation of densely packed cells using cell surface markers. Res Sq 2023. https://doi.org/10.21203/rs.3.rs-3307496/v1.

[38] Stringer C. A generalist algorithm for cellular segmentation with human-in-the-loop capabilities. https://github.com/MouseLand/cellpose. [Accessed 10 January 2024].

[39] Zhou D, Fang J, Song X, Guan C, Yin J, Dai Y, et al. IoU loss for 2D/3D object detection. In: 2019 international conference on 3D vision (3DV). IEEE; 2019. p. 85–94. https://ieeexplore.ieee.org/document/8886046.

[40] Zhou M, Li G, Zhang Z, Liang J, Tian L. Effect of ignition energy on the initial propagation of ethanol/air laminar premixed flames: an experimental study. Energy Fuels 2017;31:10023–31. https://doi.org/10.1021/acs.energyfuels.7b00965.

[41] Essmann S, Markus D, Grosshans H, Maas U. Experimental investigation of the stochastic early flame propagation after ignition by a low-energy electrical discharge. Combust Flame 2020;211:44–53. https://doi.org/10.1016/j.combustflame.2019.09.021.

[42] Zhang F, Zirwes T, Häber T, Bockhorn H, Trimis D, Suntz R. Near wall dynamics of premixed flames. Proc Combust Inst 2021;38:1955–64. https://doi.org/10.1016/j.proci.2020.06.058.

[43] Di Y, Huang Z, Zhang N, Zheng B, Wu X, Zhang Z. Measurement of laminar burning velocities and Markstein lengths for diethyl Ether−Air mixtures at different initial pressure and temperature. Energy Fuels 2009;23:2490–7. https://doi.org/10.1021/ef900015k.

[44] Bradley D, Hicks RA, Lawes M, Sheppard CGW, Woolley R. The measurement of laminar burning velocities and Markstein numbers for iso-octane–air and iso-octane–n-heptane–air mixtures at elevated temperatures and pressures in an explosion bomb. Combust Flame 1998;115:126–44. https://doi.org/10.1016/S0010-2180(97)00349-0.

[45] Kim W, Sato Y, Johzaki T, Endo T, Shimokuri D, Miyoshi A. Experimental study on self-acceleration in expanding spherical hydrogen-air flames. Int J Hydrogen Energy 2018;43:12556–64. https://doi.org/10.1016/j.ijhydene.2018.04.15303.